Engineering spin-orbit effects and Berry curvature by deposition of a monolayer of Eu on WSe_2

Johanna P. Carbone,[1,2,*] Dongwook Go,[1,3] Yuriy Mokrousov,[1,3] Gustav Bihlmayer,[1] and Stefan Blügel[1]

[1]*Peter Grünberg Institut and Institute for Advanced Simulation, Forschungszentrum Jülich and JARA, 52425 Jülich, Germany*

[2]*Physics Department, RWTH-Aachen University, 52062 Aachen, Germany*

[3]*Institute of Physics, Johannes Gutenberg University Mainz, 55099 Mainz, Germany*

(Received 5 April 2022; revised 27 June 2022; accepted 20 July 2022; published 1 August 2022)

Motivated by recent progress in two-dimensional (2D) spintronics, we present a monolayer of Eu deposited on 1H-WSe_2 as a promising platform for engineering spin-orbit effects and Berry curvature. By first-principles calculations based on density functional theory, we show that Eu/WSe_2 exhibits intriguing properties such as high magnetic anisotropy, valley-dependent polarization of spin and orbital angular momenta, and Rashba textures. These originate from magnetic and spin-orbit proximity effects at the interface and the interplay between localized $4f$ magnetic moments of Eu and mobile charge carriers of Eu and WSe_2. The analysis of the magnetic properties reveal a ferromagnetic configuration with an out-of-plane easy axis of the magnetization, which favor a pronounced anomalous Hall effect in the proposed system. Thus, we promote $4f$ rare-earth metals deposited on top of a transition-metal dichalcogenides as a promising platform for 2D spintronics.

DOI: 10.1103/PhysRevB.106.064401

I. INTRODUCTION

Transition-metal dichalcogenides (TMDCs) are two-dimensional (2D)-materials with the formula MX_2, where M is a transition-metal element bonded to chalcogen atoms X. Based on the composition (i.e., the nature of M and X) and the crystalline structure [1,2] (the stacking sequence in the bulk systems), such systems exhibit different electronic properties and can be semimetals, semiconductors, metals, or even superconductors [3–11]. Moreover, individual monolayers of TMDC are atomically thin structures, which can manifest either hexagonal (1H phase) or octahedral symmetry (1T phase) [2]. These materials exhibit interesting phenomena such as valley degrees of freedom [12] and band splitting [13] due to the presence of different features they naturally possess, like inversion symmetry breaking and strong spin-orbit coupling (SOC). The inversion symmetry breaking leads to valley-dependent orbital splittings at the corner points K and K′ of the hexagonal Brillouin zone (BZ), which are characterized by the opposite signs of the orbital angular momentum and Berry curvature. This leads to the valley-orbital Hall effect, where electrons at K and K′ valleys carry the opposite orbital angular momentum [14–19]. Furthermore, strong SOC leads to valley-dependent spin polarization and results in the spin Hall effect [20]. The valley-dependent Berry curvature also leads to the Berry curvature dipole, which drives a nonlinear Hall effect [21–24].

In recent years, different studies have been conducted on TMDCs, showing that the symmetry properties have an important impact on the transport properties. In Ref. [25], it is demonstrated that by application of an electric field perpendicular to a WSe_2 bilayer, structural inversion symmetry is broken and it is thus possible to control the Berry curvature and the orbital moment at the K and K′ valleys by tuning the external electric field. Reducing the system to a monolayer, different kinds of SOC effects arise due to the reduction in symmetry which can be exploited in valleytronics as explained in Ref. [26].

By proximity effect, it is also possible to induce exchange interaction by depositing a ferromagnetic layer on top of a TMDC. Since a clean surface of TMDCs can be prepared by exfoliation, it can be brought into intimate contact with a ferromagnet [27]. It is found that these magnetic interactions modify the extent of the Hall effects compared to the situation without exchange interaction [28].

The coexistence of strong SOC, emerging from the transition metal of a TMDC monolayer, and of a net magnetization is also the key ingredient for magnetotransport phenomena such as the anomalous Hall effect (AHE) [29] and spin-orbit torque [30,31]. In particular, the low symmetry of the TMDCs can induce unconventional spin polarization and torque [30,32,33], which is crucial for field-free magnetization switching.

By similar reasoning, the presence of rare-earth adatoms with high coverage on top of TDMCs is here demonstrated to produce an additional contribution to the Hall conductivity that depends on the particular topology of the band structure and can be described in terms of Berry curvature. The combination of rare-earth atoms with 2D materials is a promising strategy for the implementation of novel magnetic storage devices and for applications in the field of spintronics. Indeed, the use of rare-earth atoms as a magnetic source has different advantages, such as high magnetic moments generated by localized $4f$ electrons, the effect of which, together with the strong SOC and the particular crystal field of the 2D material, generates a magnetocrystalline anisotropy that is intensively studied from both theoretical and experimental point

*j.carbone@fz-juelich.de

of view [34–38]. This effect can be exploited for example in the creation of nanoscale magnets where the main challenge is the stabilization of the magnetic moments which undergo fluctuations due to vibrations or interaction with conduction electrons of the substrate. This can be achieved in several ways, for instance, through manipulation of the symmetry properties of the system.

In the present work, the effect of the adsorption of one monolayer of Eu atoms on a WSe_2 substrate modeled by one layer of formular unit in the 1H phase is investigated through *ab initio* density functional theory (DFT) calculations. We calculate the lowest energy magnetic state covering all Heisenberg-type interactions by scanning energies of the spin-spiral state for **q** vectors across the Brillouin zone and determine the magnetic anisotropy energy. We predict for a Eu monolayer on WSe_2 a ferromagnetic out-of-plane magnetic state. We compare the results to a structural model with 1/3 Eu coverage. A further analysis concerns the impact of the $4f$ metal on the spin-orbital texture and on the consequences of the interaction between the rare-earth electrons and the substrate on the band topology. In particular, anomalous Hall transport properties are analyzed by considering a high coverage of the $4f$ metal and using interpolation by Wannier interpolation. It is shown that the adsorption of Eu generates states in the gap of the semiconducting substrate, which are influenced by the SOC arising from the W atom and that hybridization between the different species induces a nontrivial Berry curvature and an anomalous Hall conductivity, which is experimentally measurable.

II. RESULTS

A. Computational details

WSe_2 has a hexagonal structure characterized by one W atom covalently bonded to six Se atoms. To determine the adsorption site for the atom in the Eu monolayer, we compare the total energies of the three different sites: on top of the W atom (T-W), on top of the Se atom (T-Se), and in the middle of the hexagon formed by W and Se atoms (H). The relaxation procedure and the following calculations are performed inside of a 1×1 simulation cell with lattice constant $a = 3.327$ Å using the full-potential linearized augmented plane-wave (FLAPW) method as implemented in the FLEUR code [39] and using DFT plus Hubbard U method [40] in order to account for the highly localized $4f$ electrons. In this respect, the Perdew-Burke-Ernzerhof exchange-correlation functional [41] is adopted and the on-site Coulomb and Hund exchange parameters are set to $U = 6.7$ eV and $J = 0.7$ eV, which are values widely accepted for the treatment of f electrons in chemical elements with half-filled $4f$ shells such as Eu and Gd [40,42] as with those structural, thermodynamic, and electronic structure data are reproduced well.

Concerning the computational parameters, we set the muffin-tin radii to $2.80\,a_0$ for Eu and $2.29\,a_0$ for W and Se, where a_0 is the Bohr radius. The cut-off for the plane-wave basis functions is chosen to be $K_{\max} = 4.0\,a_0^{-1}$ for the wave functions and $G_{\max} = 10.7\,a_0^{-1}$ for the charge density and potential. The upper limit of angular momentum inside of the muffin-tin sphere is set to $l_{\max} = 10$ for Eu and $l_{\max} = 8$ for W and Se. For the self-consistent field cycle, a 10×10 **k**-point mesh is sampled throughout the first Brillouin zone. For the calculation of the magnetic anisotropy curve and the spin-spiral discussed in Sec. II C, we adopted a 21×21 **k**-point mesh. Concerning the spin-polarized calculations for the $\sqrt{3} \times \sqrt{3}$ simulation cell discussed in Sec. III A, the same computational, on-site, Coulomb and Hund exchange parameters have been used, but a 20×20 **k**-point mesh has been adopted.

TABLE I. Adsorption energy, distance of the Eu atom from the WSe_2 layer, the magnetic moment, and the f and d occupations in the muffin-tin sphere of the Eu atom for the different adsorption sites of Eu in the 1×1 unit cell. Calculations have been performed without SOC.

Site	E_{ads} (eV)	h (Å)	m_s^{tot} (μ_B)	f_{occ}	d_{occ}
H	−0.312	2.830	7.240	6.861	0.520
T-W	−0.474	2.500	7.130	6.865	0.522
T-Se	−0.341	3.119	7.440	6.858	0.550

Table I summarizes the adsorption energy of the Eu monolayer atom on each adsorption site, the distance along the z direction, i.e., perpendicular from the top Se layer, the magnetic moment of Eu, and the f and d occupations in the valence shell of Eu for the unit cell shown in Fig. 1. The reference point of the energy is defined as the total energy for an isolated Eu monolayer and WSe_2. In the case of T-Se, h represents the distance between the Eu atom and the Se atom, which is directly underneath the Eu one. From these data, it is evident that the most stable adsorption site is Eu on top of the W atom (Fig. 1) and that the $4f$ metal maintains its large magnetic moment of about 7.1 μ_B independent of the structural details. Looking at the occupation numbers of the $4f$ electrons of Eu, f_{occ}, we find a value close to the atomic limit of 7 $4f$ electrons and consistent with Hund's first rule of half-filled shells, we find $4f$ magnetic moments of $m_{4f} = f_{\text{occ}}$, which explains the large magnetic moments. Such a value is close to what is obtained by adopting the Hubbard-I approximation in the calculation of bulk Eu [43]. The small deviation from the theoretical atomic value of 7 μ_B suggested by Hund's rule, arises primarily from the Eu d electrons, which become spin polarized due to the intra-atomic exchange interaction between the $4f$ and $5d$ electrons. For the lowest energy Eu stacking on WSe_2 we estimate the magnetic moment of the Eu d electrons to $m_{5d} = m_s^{\text{tot}} - f_{\text{occ}} \approx 0.265\ \mu_B$.

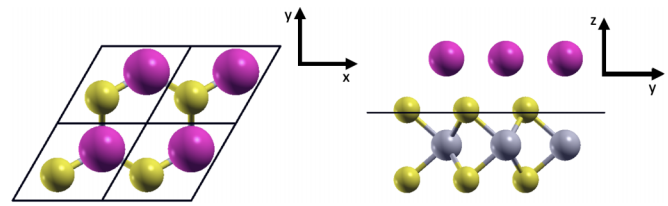

FIG. 1. Structure of the 1×1 unit cell of Eu (purple spheres) monolayer deposited on top of the W atom (gray spheres) of a single layer of WSe_2. Se atoms are indicated by yellow spheres.

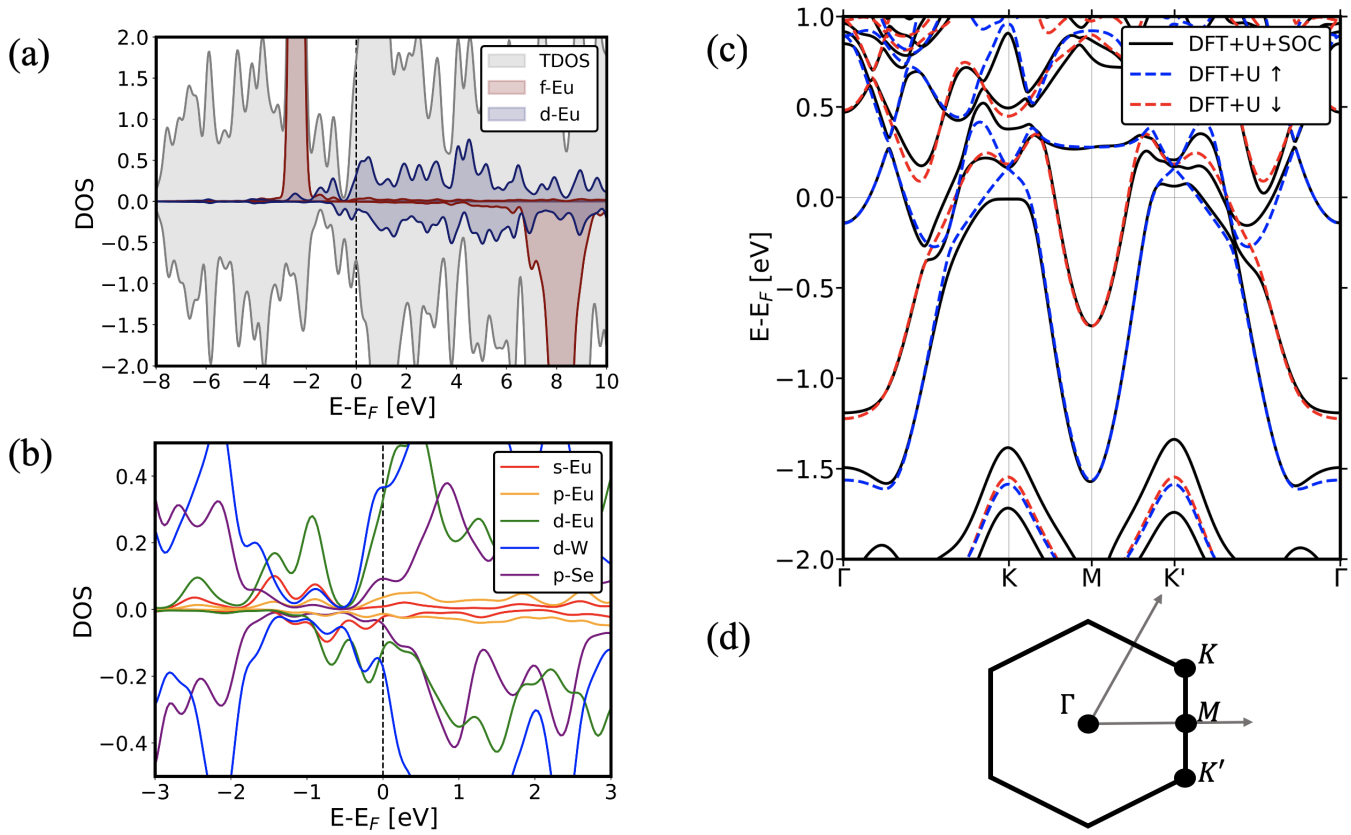

FIG. 2. (a) Contribution to the local DOS of the f and d electrons of Eu. The total DOS (TDOS) is shown as gray shaded area. (b) Contribution to the local DOS of the s, p, d electrons of Eu, d electrons of W, and p electrons of Se. Both DOS in panels (a) and (b) have been calculated without SOC. (c) Band structure of Eu/WSe_2 calculated with DFT+U (blue dashed line represents the majority channel and red dashed line represents the minority channel) and with DFT+U+SOC (black solid line). (d) First Brillouin zone with high-symmetry points.

The DFT energy bands are compared to the band structure obtained by constructing maximally localized Wannier functions (MLWFs) in the FLAPW formalism [44] and the open-source code Wannier90 [45]. The initial projections for the Wannier functions are chosen to be s, d, f orbitals for the Eu atom, p orbitals for the Se atoms, and s, d orbitals for the W atom. In this way, 50 MLWFs are constructed, where the frozen window maximum was set 0.4 eV above the Fermi energy. From the converged MLWFs, the Hamiltonian, spin, and orbital operators are written in real space, which is Fourier transformed in an interpolated **k** mesh for the calculation of spin-orbital texture, Berry curvature, and AHE.

B. Electronic structure

A detailed analysis of the electronic structure, the orbital contribution, and hybridization effects occurring in the system can be found in the Supplemental Material [46] visualized in Figs. S1 and S2. One immediately notices that unlike the pristine WSe_2 substrate monolayer, the system is metallic. In first approximation, we can understand the electronic structure of our system by the electronic structure of the WSe_2 monolayer to which Eu donates spin-polarized conduction electrons through hybridizaton and subsequently the Fermi surface cuts now into the formerly unoccupied WSe_2 conduction states. Thus, in the vicinity of the Fermi surface we observe spin-polarized Eu d (and s) states hybridizing with W d states. In addition, it is evidenced that the valley-shaped states at -1.5 eV at the K and K′ points, which have predominantly d character from W, split in the presence of SOC. In the following, we focus on the discussion of spin polarization, SOC, and hybridization effects of the Eu/WSe_2 system.

The effect of the interactions between the Eu atom and the substrate can be understood by looking at the electronic structure of the material, shown in Fig. 2. An overview of the spin-resolved electronic structure is obtained from Fig. 2(a) which displays the total DOS (TDOS) and the d- and f-orbital resolved local density of states (LDOS) of Eu. The upper (lower) panel, DOS $\geqslant 0$ ($\leqslant 0$), denotes the majority (minority) states. We observe the $4f$-majority states of Eu, fully occupied with about seven electrons, energetically localized at around -2.5 eV, and the unoccupied minority ones at about $+8$ eV, exhibiting an exchange splitting of about 11 eV. The Eu d states are largely unoccupied, illustrating a large bandwidth over more than 10 eV, a result of the large delocalization of theses states. A small fraction of the Eu d electrons are occupied consistent with $d_{\mathrm{occ}} = 0.522$ in Table I, this being a consequence of the hybridization with neighboring atoms that the Eu atom undergoes when it becomes part of the solid phase instead of being an isolated single atom. This hybridization promotes the Eu s electrons to d electrons. To understand the strength of this effect, it is interesting to compare the Eu $s \rightarrow d$ promotion to the case of the quasisingle Eu atom adsorption discussed in Sec. III A and summarized in Table II.

TABLE II. Adsorption energy, distance of the Eu atom from the WSe_2 layer, the magnetic moment, and the f and d occupations in the muffin-tin sphere of the Eu atom for the different adsorption sites in the $\sqrt{3} \times \sqrt{3}$ cell.

Site	E_{ads} (eV)	h (Å)	m_s^{tot} (μ_B)	f_{occ}	d_{occ}
H	−0.611	2.582	6.991	6.923	0.128
T-W	−0.690	2.500	6.994	6.923	0.158
T-Se	−0.401	3.112	7.000	6.922	0.085

One clearly witnesses that the TDOS of the majority and minority states are different, especially in the vicinity of the Fermi energy. Therefore, we focus in Fig. 2(b) on the spin- and orbital-resolved LDOS of Eu (s, p, d), W-d and Se-p, in the energy window of ±3 eV around the Fermi energy. Please notice the scale of the DOS is finer by a factor of 4 than that in Fig. 2(a) and the Eu-4f LDOS is neglected. We find the LDOS is dominated by the Eu-d, W-d, and Se-p states. It is seen that in this energy window W-d hybridizes with Se-p states. The strongest exchange splitting of about 1.7 eV is found for the Eu-d states, resulting finally in the magnetic Eu d-electron moment of 0.265 μ_B as discussed in the context of Table I. This is a result of the intra-atomic ferromagnetic exchange coupling between the localized Eu-4f and the delocalized d states. In the direct vicinity of the Fermi surface (±0.5 eV) one observes a strong spin dependence of Eu-d, W-d, and Se-p DOS. Clearly the majority states dominate over the minority states and one finds a hybridization between the W and Eu d states.

The role of the spin-orbit coupling is analyzed in Fig. 2(c), displaying a comparison between the spin-resolved band structure in the vicinity of the Fermi energy along high-symmetry lines [for details see Fig. 2(d)], neglecting the SOC by which majority states (blue lines) and minority states (red lines) are well-defined eigenstates with the ones calculated with SOC (black lines). A strong spin-orbit splitting is witnessed at the K and K′ points around −1.6 eV. These primarily W d states spin-orbit split by about ±0.18 to −1.42 and −1.78 eV into $j = 3/2$ and $j = 5/2$ states. In the same way, also the crossing point at K just above the Fermi energy is split up into two separated bands, while on the path between K and Γ just below the Fermi energy an avoided crossing is generated. This plays a crucial role in determining the strength of the magnetic anisotropy, in generating large Berry curvature and contributing to the AHE. Concerning the energy bands from K′ to Γ, similar effects arise but it can be already noticed that the two high-symmetry points K and K′ are not equivalent due to the absence of structural inversion symmetry. As anticipated from the large LDOS of W-d at the Fermi energy, discussed in Fig. 2(b), in general, the SOC effect arises mainly from the W atom.

C. Perpendicular magnetic anisotropy

In magnetic data-storage devices, an important key ingredient is the stiffness of the magnetization with respect to external perturbations (i.e., thermal fluctuations or scattering from conduction electrons) such that a specific direction of the magnetic moments is stable over time, which translates into the need for high magnetic anisotropy energies. This is particularly important in thin film magnets, where high magnetic anisotropy can circumvent the Mermin-Wagner theorem in 2D [47,48]. In Fig. 3(a), the total energy of Eu/WSe_2 is plotted with respect to the angle θ between the surface normal direction and the direction of the magnetization. The result indicates an out-of-plane easy axis of the magnetization ($\theta = 0°$) as minimum energy state with an energy difference of 1.75 meV per unit cell compared to the energy of the in-plane state.

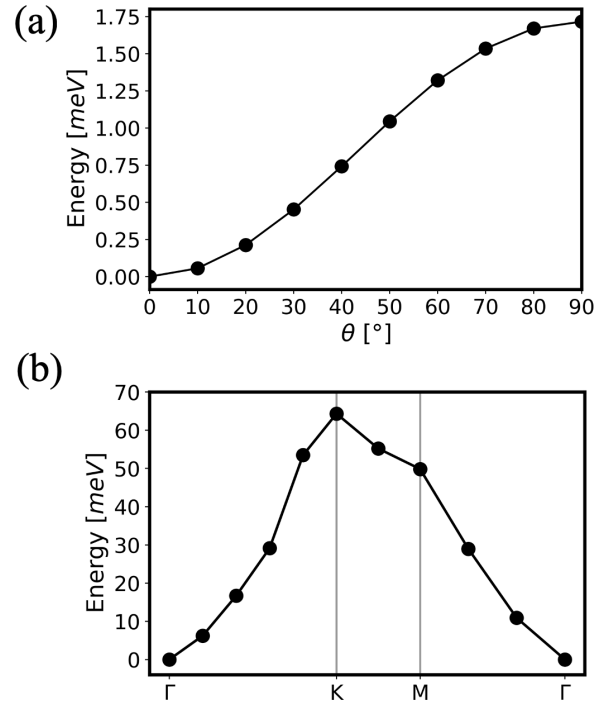

FIG. 3. (a) Magnetic anisotropy energy curve: the total energy of the system plotted vs the polar angle θ of the magnetization measured from the z axis. (b) The energy of the spin-spiral states of a flat spiral, i.e., with cone angle $\beta = \pi/2$, computed for the values of the $\mathbf{q}$ vector along the Γ-K-M path, presented with respect to the ferromagnetic ground state at the Γ point.

This effect can be described in terms of the magnetic anisotropy emerging from the electronic hybridization between Eu and WSe_2. Eu has 7 4f electrons, leading to a closed-shell situation for which the total orbital angular momentum is $L = 0$, but the total spin moment is close to 7 μ_B as discussed before. Therefore, we expect no direct magnetic anisotropy from the 4f shell. On the other hand, we discussed in Sec. II B the ferromagnetic spin polarization of the Eu-d electrons due to intra-atomic exchange with 4f electrons as well as the hybridization of the Eu and W d electrons at the Fermi surface. By comparing in Fig. 2(c) the band structure with and without SOC, we witness a strong SOC influence on the Eu-W hybridization at the Fermi energy. Turning the spin-quantization axis of the Eu-4f electrons, the spin-quantization axis of the Eu-d electrons will follow and the spin-orbit dependent interaction between the spin-quantization axis of the Eu-d states with the crystal lattice dependent spin-orbit interaction of the W-d electrons will lead to the magnetic anisotropy energy observed in Fig. 3(a).

D. Magnetic order

To confirm that the magnetic ground state is indeed an out-of-plane ferromagnetic phase, we study the total energy for a given spin-spiral state with wave vector $\mathbf{q}$ (defined in units of the reciprocal lattice vectors) along the high-symmetry lines in the 2D Brillouin zone. Recall that the spin spiral is the exact mathematical solution of the classical Heisenberg model applied to periodic crystal lattices within the set of all single-$\mathbf{q}$ states [49]. The $\mathbf{q}$-state with the lowest energy, is then the magnetic ground state among all Heisenberg-type interactions. Based on symmetry arguments, we expect the minimum energy to be found either at high-symmetry points, or at high-symmetry lines between high-symmetry points. The high-symmetry points of the Brillouin zone then correspond to a certain periodic magnetic order in the real space (for hexagonal lattices, see Ref. [50]). A numerically very efficient method to calculate the DFT total energy for a spin-spiral state is the generalized Bloch theorem [51,52] as implemented in the FLEUR code [53]. Figure 3(b) shows the energy calculated for different values of the $\mathbf{q}$ vector of a spin spiral along the Γ-K-M path. The first Brillouin zone is shown in the inset in Fig. 2(b), highlighting the high-symmetry points. We find the energy minimum at Γ, indicating that the system favors a ferromagnetic ground state. Furthermore, the energy differences between the Γ and the other two high-symmetry points, K (noncollinear 120°-Néel state) and M (row-wise antiferromagnetic state) are about 70 and 50 meV. Therefore, the Néel or the antiferromagnetic state is not energetically favorable.

E. Orbital and spin textures

In a TMDC monolayer, spatial inversion symmetry is broken, and the immediate consequence is the emergence of inequivalent valleys K and K′ in $\mathbf{k}$ space. This leads to valley-dependent orbital angular momentum and Berry curvature and results in the valley-orbital Hall effect [16,18,19]. Additionally, by depositing Eu atoms on WSe_2, the Rashba effect can be induced by breaking the mirror symmetry with respect to the 2D plane [54,55]. The Rashba effect is induced not only on the spin but also on the orbital angular momentum, which is known as the orbital Rashba effect [56–59]. These spin and orbital textures play a crucial role in spin and orbital magneto-transport phenomena [17,60,61].

Thus, we investigate the spin, $\mathbf{S}_{\mathrm{FS}}(\mathbf{k})$, and orbital, $\mathbf{L}_{\mathrm{FS}}(\mathbf{k})$, texture in $\mathbf{k}$ space at the Fermi surface of Eu/WSe_2. Following Ref. [61], the latter

$$\mathbf{L}_{\mathrm{FS}}(\mathbf{k}) = \sum_n \frac{2\,\langle u_{n\mathbf{k}}|\,\mathbf{L}\,|u_{n\mathbf{k}}\rangle}{1+\cosh[(E_{\mathrm{F}}-E_{n\mathbf{k}})/k_{\mathrm{B}}T]} \tag{1}$$

is evaluated as expectation value of the orbital angular momentum operator $\mathbf{L}$ defined within the muffin-tin sphere of each atom $u_{n\mathbf{k}}$ is the periodic part of the Bloch state with band index n. The denominator expresses the Fermi-Dirac temperature broadening of the Fermi surface. We set $k_{\mathrm{B}}T = 25$ meV for broadening, where k_{B} is the Boltzmann constant and T is the temperature. $E_{n\mathbf{k}}$ corresponds to the energy band and E_{F} to the Fermi energy. The spin texture is obtained replacing $\mathbf{L}$ by $\mathbf{S}$ in (1).

The k-space-dependent spin and orbital texture at the Fermi surface is summarized in Fig. 4. Overall, we find that $\mathbf{S}_{\mathrm{FS}}$ and $\mathbf{L}_{\mathrm{FS}}$ are of the same order of magnitude and thus neither are good quantum numbers. It is a result of a competition of the intra-atomic $\langle \mathbf{S_z}\rangle_{\mathrm{FS}}$ and $\langle \mathbf{L_z}\rangle_{\mathrm{FS}}$ polarization of Eu s and d states due to the Eu $4f$ electrons and the hybridization with W d-electrons subject to strong orbital-dependent Rashba-type SOC.

Figure 4(a) shows the z component of the orbital angular momentum. We find a threefold rotational symmetry, as expected, and the valley-dependent orbital texture is observed, which have opposite signs at K and K′ valleys. We find that this feature is similar to the conduction states of the bare WSe_2 [62]. The z component of the spin angular momentum is shown in Fig. 4(c). Although it satisfies a threefold rotation symmetry, it nearly exhibits a sixfold rotation symmetry. This is because the spin magnetism is mainly driven by Eu layer, which has a sixfold rotation symmetry if the substrate is absent. Slight deviation of the spin texture from the sixfold rotation symmetry indicates hybridization of Eu atoms with the substrate, where proximity-induced W d states exhibit finite spin polarization via an indirect exchange interaction between itinerant Eu s, d electrons, and the spin moments of localized f electrons. These features can be directly associated to the orbital contributions to the band structure discussed in Fig. 2(c) and in the Supplemental Material (Fig. S1). Here, around the Γ point the Eu-d majority states are prevalent. This leads to the positive value of $\langle S_z\rangle_{\mathrm{FS}}$ around the Γ point.

Concerning the K and K′ points instead, the biggest contribution comes from the W-d states with a spin-orbit splitting that competes in energy with the exchange splitting of the hybridizing s and d electrons of Eu, causing the majority states to lie around the Fermi energy and a full quantum mixture of electronic states, resulting in three-dimensional spin and angular moment textures. Comparing Figs. 4(a) to 4(d) around the K and K′ points, we indeed observe similar values for $\langle \mathbf{S}\rangle_{\mathrm{FS}}$ and $\langle \mathbf{L}\rangle_{\mathrm{FS}}$ for the out-of-plane and in-plane components, respectively.

Figure 4(b) shows the in-plane component of the orbital angular momentum, $\langle L_{xy}\rangle_{\mathrm{FS}} = \sqrt{\langle L_x\rangle^2_{\mathrm{FS}} + \langle L_y\rangle^2_{\mathrm{FS}}}$, which captures a chiral Rashba-like texture. Here, the *orbital* Rashba effect originates from the hybridization between Eu and WSe_2, which breaks the z-reflection mirror symmetry. We note that the orbital Rashba effect emerges regardless of the SOC and it is a consequence of the orbital hybridization [58]. When the SOC is taken into account, the chiral orbital texture is accompanied by the chiral spin texture, leading to the emergence of *spin* Rashba effect, Fig. 4(d). We note the stark resemblance of the in-plane orbital and spin textures, which supports the idea that both share the same origin—the orbital hybridizations. This also explains why a threefold rotation symmetry is evident in both spin and orbital textures for the in-plane components, compared to those for the out-of-plane component.

F. Berry curvature

The features of the spin-orbital texture and the perpendicular magnetization arranged in a ferromagnetic fashion

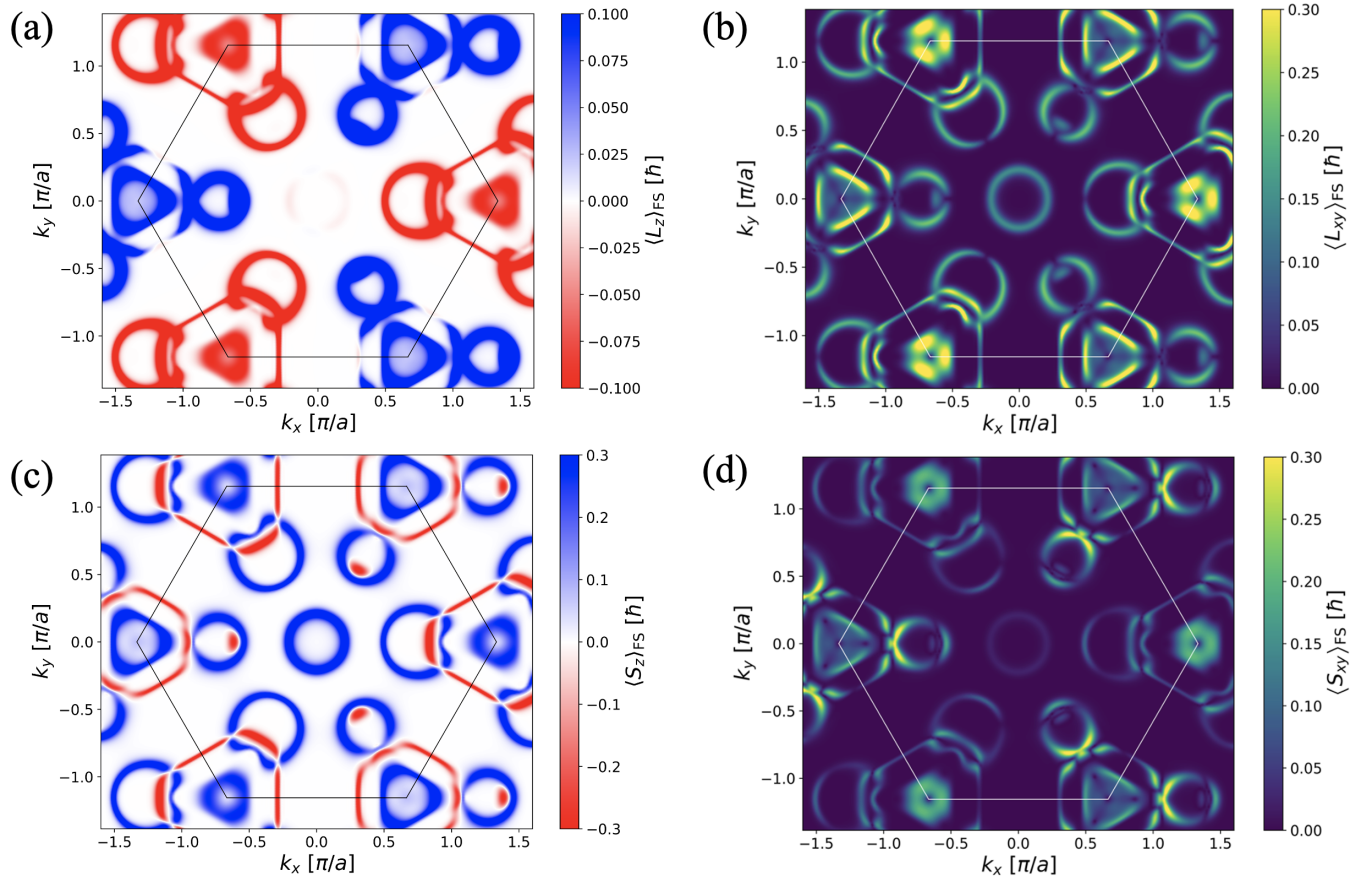

FIG. 4. Spin and orbital texture in **k** space at the Fermi surface. (a) Expectation value for the out-of-plane component of the orbital angular momentum at the Fermi surface $\langle L_z \rangle_{\rm FS}$. (b) Magnitude of the expectation value of the in-plane component of the orbital angular momentum $\langle L_{xy} \rangle_{\rm FS} = \sqrt{\langle L_x \rangle_{\rm FS}^2 + \langle L_y \rangle_{\rm FS}^2}$. Analogously, the z component and the magnitude of the in-plane component for the spin expectation value at the Fermi surface are shown in panels (c) and (d), respectively. $\langle L_z \rangle_{\rm FS} > (<) 0$ and $\langle S_z \rangle_{\rm FS} > (<) 0$ [color blue (red)] correspond to the angular-momentum direction (anti)parallel to the spin of Eu-4f electrons.

are an interesting starting point for the investigation of the anomalous conductivity. The latter can be described in terms of Berry curvature, which acts in **k** space as an effective magnetic field and causes a transverse electron current in presence of an electric field. The Berry curvature is evaluated using the Kubo formula,

$$\begin{aligned}\Omega_{n\mathbf{k}} &= \partial_{k_x} A^y_{n\mathbf{k}} - \partial_{k_y} A^x_{n\mathbf{k}} \\ &= -2\mathrm{Im}[\langle \partial_{k_x} u_{n\mathbf{k}} | \partial_{k_y} u_{n\mathbf{k}} \rangle] \\ &= -2\hbar^2 \sum_{m \neq n} \mathrm{Im}\left[\frac{\langle u_{n\mathbf{k}} | \, v_x \, | u_{m\mathbf{k}} \rangle \, \langle u_{m\mathbf{k}} | \, v_y \, | u_{n\mathbf{k}} \rangle}{(E_{n\mathbf{k}} - E_{m\mathbf{k}} + i\eta)^2} \right], \end{aligned} \quad (2)$$

where $\Omega_{n\mathbf{k}}$ is the Berry curvature for a Bloch state with band index n with finite scattering (η), $\mathbf{A}_{n\mathbf{k}} = i \langle u_{n\mathbf{k}} | \partial_{\mathbf{k}} u_{n\mathbf{k}} \rangle$ is the Berry connection, and $v_{x(y)}$ is the $x(y)$ component of the velocity operator. The room temperature broadening is introduced by a small positive number η, which is set to 25 meV. A lower (higher) temperature or η, respectively, will lead to more (less) spiky variations of the Berry curvature in momentum space. From Eq. (2), it is clear that there will be contributions to the Berry curvature from the regions where the energy bands are separated by small energy gaps by the effect of SOC, such as avoided crossings discussed in Fig. 2(a).

While the Berry curvature vanishes when the spatial inversion and time-reversal symmetries are combined, in Eu/WSe_2 both symmetries are broken. In particular, orbital hybridizations by proximity and the SOC can generate strong Berry curvature near avoided crossings of bands as shown in Fig. 2(a). This explains the features of the Berry curvature shown in Fig. 5(a), where the calculated band structure along the **k** path Γ-K-M-K′-Γ and the respective value is shown in color scale. Different hot spots of $\Omega_{n\mathbf{k}}$ can be seen at points where the SOC lifts the degeneracy of the energy bands. In particular, the splitting of the bands between Γ and K appears to result in a band inversion. In terms of Eq. (2), these splittings correspond to small values of the denominator and thus sharp peaks of the Berry curvature. In Fig. 5(b), we show the Berry curvature summed over all occupied states below the Fermi energy for the same **k** path. We confirm that spiky contributions comes from the SOC-induced avoided crossings, which is found on Γ-K and Γ-K′ paths. Another important feature is that also in terms of Berry curvature, the two K and K′ points are inequivalent: The K point presents a positive peak, while at the K′ point displays a broad negative feature. Along the path K′-Γ, an intense peak appears characterized by inverted sign with respect to the peak between Γ-K.

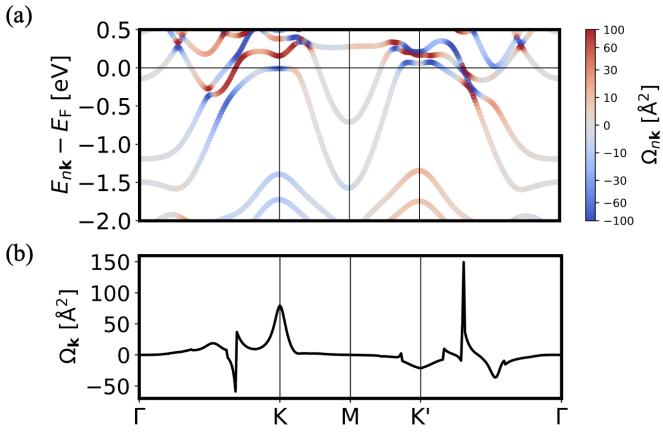

FIG. 5. (a) Band structure around the Fermi energy with color scale indicating the value of the Berry curvature $\Omega_{n\mathbf{k}}$. (b) Berry curvature summed over all occupied states along the **k** path Γ-K-M-K′-Γ.

G. Anomalous Hall effect

By integrating the Berry curvature over the Brillouin zone (BZ), it is possible to calculate the intrinsic anomalous Hall conductivity as

$$\sigma_{\mathrm{AH}} \equiv \sigma_{yx} = \frac{e^2}{\hbar} \sum_n \int_{\mathrm{BZ}} \frac{d^2k}{(2\pi)^2} f_{n\mathbf{k}} \Omega_{n\mathbf{k}}, \tag{3}$$

where $f_{n\mathbf{k}}$ is the Fermi-Dirac distribution function evaluated at room temperature, i.e., at 25 meV. Figure 6 shows the anomalous conductivity σ_{yx} as a function of the Fermi energy. The Fermi energy is varied with respect to the original value $E_{\mathrm{F}}^{\mathrm{true}}$ by assuming that the potential is fixed for the change of band filling. Major peaks are found around 2 eV below the Fermi energy, slightly above the Fermi energy, and 1 eV above the Fermi energy. These energies are where avoided band crossings induced by the SOC are found. A double-peak feature right above the Fermi energy implies an interesting possibility to tune the Hall response by electron doping, which may be

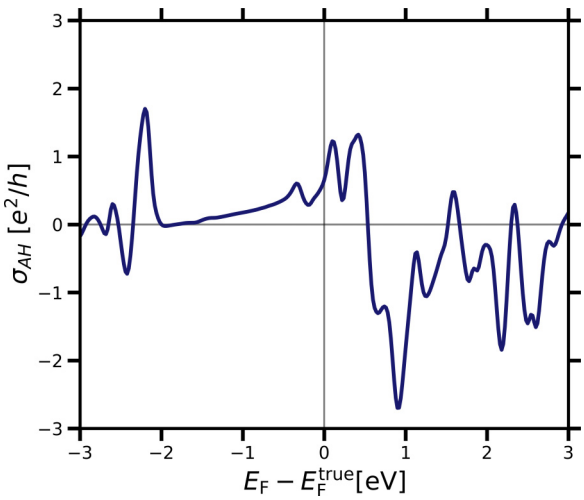

FIG. 6. Anomalous Hall conductivity as a function of the Fermi level.

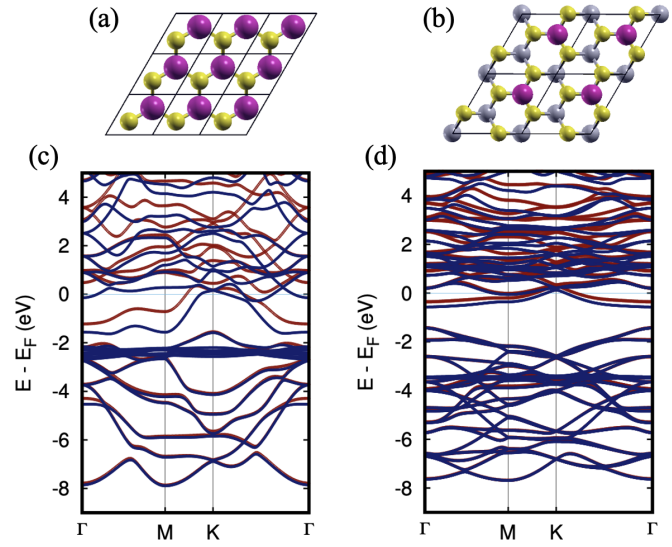

FIG. 7. Comparison of the electronic structure of Eu monolayer on WSe_2 monolayer for two simulation cells: (a) 1×1 unit cell (high coverage of Eu) and (b) $\sqrt{3} \times \sqrt{3}$ unit cell (low coverage of Eu). The corresponding band structures determined neglecting SOC are shown in panels (c) and (d), where blue and red lines indicate majority and minority states, respectively.

experimentally observed. Meanwhile, the peak at −2 eV is where the K and K′ valleys of WSe_2 in **k** space are situated. From Fig. 2(a) it is clear that SOC lifts the degeneracy of the band at the K and K′ valleys which have predominantly d character from the W atom such that a contribution to the Berry curvature arises.

III. DISCUSSION

A. Effect of Eu coverage

In an experimental setup, Eu atoms might not fully cover the WSe_2 substrate. To investigate the effect of Eu coverage on the electronic and magnetic properties, we also compare the electronic structures of Eu in the 1×1 unit cell [see Fig. 7(a)] with Eu in the $\sqrt{3} \times \sqrt{3}$ unit cell [Fig. 7(b)], in which Eu has 1/3 coverage compared to the 1×1 unit cell. Table II summarizes the adsorption energies, distances from the substrate (as discussed also in Sec. II A), the total magnetic moment of the Eu atom, its f- and d-state occupation for the $\sqrt{3} \times \sqrt{3}$ cell. In this dilute situation with respect to Eu coverage, we witness that Eu is much more in the limit of single-atom adsorption: The adsorption energy is slightly increased (the bonding toward the substrate is stronger), the occupation number of the Eu f electrons is approaching the atomic number of 7, the occupation number of the Eu d electrons, d_{occ}, is a factor of 4 smaller, and the magnetic moment of the Eu d electrons $m_d \approx 0.07\ \mu_{\mathrm{B}}$ is a factor of 3 smaller, when compared to the dense coverage.

Obviously, reducing the Eu coverage of WSe_2 reduces the magnetic proximity of WSe_2 by decreasing the hybridization of Eu and W d electrons and, at the same time, the semiconducting features of the WSe_2 monolayer reemerges. Inspecting the band structure of $(\sqrt{3} \times \sqrt{3})$-Eu/$WSe_2$ in Fig. 7(d), we observe a band gap of about ±0.4 eV at around

−1 eV. The doping of WSe_2 by Eu s, p, and d electrons makes $(\sqrt{3} \times \sqrt{3})$-Eu/$WSe_2$ a conductor. Comparing the exchange splitting of the states at the Fermi energy (energy difference between the red and blue lines) with those of the full coverage case in Fig. 7(c), we find that the exchange splitting and thus the magnetic proximity is indeed much smaller. Figure S3 of the Supplemental Material displays the respective magnetic anisotropy energy as function of the magnetization direction in the dilute situation. In agreement with the full-coverage case, the easy axis is out of plane and consistent with our explanation given in Sec. II C that the hybridization of spin carrying Eu and the spin-orbit carrying W d electrons are the origin of the magnetocrystalline anisotropy, and the energy of the in-plane hard axis is only 0.2 meV per $\sqrt{3} \times \sqrt{3}$ unit cell, much smaller than the 1.75 meV in the 1×1 unit cell. This observation also has strong implications for realizations in experiments and suggests that a high coverage of Eu atoms is crucial for the measurement of the AHE. This also implies that the AHE should be enhanced with increasing coverage by Eu atoms.

B. Other rare-earth elements

In order to tailor an efficient device, it is necessary to protect the perpendicular magnetization from perturbations that might flip it to in-plane. An enhancement of the anisotropy energy might be obtained, for example, by substituting Eu with an open $4f$-shell rare-earth metal (such as Nd, Dy, or Ho) where the charge cloud presents deviations from the spherical geometry and electron correlations play an important role. In these cases, the $4f$ shell gives rise to an anisotropic charge cloud that depends on the nonvanishing orbital angular momentum L. The large values of L and S are a source of SOC and cause magnetocrystalline anisotropy, which can be exploited when placed in specific chemical environments. The task is to engineer properly the rare-earth/2D material combination in order to achieve high energy differences between different magnetic states. A theoretical challenge is to achieve an accurate description of open-shell $4f$ systems for which approaches like DFT+U, self-interaction corrected DFT [63], or dynamical mean field theory in the Hubbard-I approximation [37,38,43,64] that has been implemented in recent times in several codes and applied to a variety of rare-earth systems. These approaches serve as future topics of investigation.

IV. CONCLUSION

In conclusion, we analyzed the effect of depositing Eu monolayers with full and 1/3 coverage on a layer of WSe_2 and showed how the interplay of proximity-induced orbital hybridization, SOC, magnetism, and broken symmetry leads to the possibility of engineering the magnetic anisotropy, the spin-orbital texture, and the Berry curvature in such heterostructures. We explained that the large local magnetic $4f$ moment of Eu spin polarizes the delocalized Eu-d electrons which hybridize with spin-orbit carrying W-d electrons and determine such the spin-orbit properties at the Fermi surface. We predicted that these hybridization effects give rise to a magnetic anisotropy energy of about 1.75 meV, which acts as a barrier against turning the magnetization from out of plane to in plane. In addition, the analysis of the magnetic texture of the material predicts a ferromagnetic configuration among all possible magnetic states described by Heisenberg-type interactions. As a consequence of the synergy between these magnetic features and the particular spin-orbital texture, Berry curvature hot spots are induced in **k** space, which in turn lead to a sizable anomalous Hall conductivity in the sample. Such rare-earth-based properties expand the design portfolio of potential future spintronic or quantum spintronic devices using 2D materials. Indeed, a fundamental understanding of the magnetic behavior of rare-earth magnets in different 2D environments could provide the foundations for novel materials, for example, for applications in quantum computing, along the lines of ideas already being explored on rare-earth ions in molecular magnets [65]. From this point of view, also in a solid matrix, rare-earth atoms appear to be very promising and are being intensively investigated [66–68].

ACKNOWLEDGMENTS

We acknowledge Gregor Michalicek for giving advice on first-principles calculations. The project is funded by the Deutsche Forschungsgemeinschaft (DFG) through CRC 1238, Control and Dynamics of Quantum Materials: Spin orbit coupling, correlations, and topology (Project No. C01). D.G. and Y.M. acknowledge funding by the DFG through TRR 288-422213477 (Project No. B06). We acknowledge computing resources granted by RWTH Aachen University under Project No. jara0219 and by the Jülich Supercomputing Centre under Project No. jiff40.

[1] J. Kim and Z. Lee, Appl. Microscopy **48**, 43 (2018).
[2] D. Voiry, A. Mohite, and M. Chhowalla, Chem. Soc. Rev. **44**, 2702 (2015).
[3] A. Kuc, N. Zibouche, and T. Heine, Phys. Rev. B **83**, 245213 (2011).
[4] J. Wilson and A. Yoffe, Adv. Phys. **18**, 193 (1969).
[5] K. F. Mak, C. Lee, J. Hone, J. Shan, and T. F. Heinz, Phys. Rev. Lett. **105**, 136805 (2010).
[6] Y. Ding, Y. Wang, J. Ni, L. Shi, S. Shi, and W. Tang, Phys. B: Condens. Matter **406**, 2254 (2011).
[7] N. E. Staley, J. Wu, P. Eklund, Y. Liu, L. Li, and Z. Xu, Phys. Rev. B **80**, 184505 (2009).
[8] C. Ataca, H. Şahin, and S. Ciraci, J. Phys. Chem. C **116**, 8983 (2012).
[9] Y. Li, K.-A. N. Duerloo, K. Wauson, and E. J. Reeda, Nat. Commun. **7**, 10671 (2016).
[10] A. Ciarrocchi, A. Avsar, and D. E. A. Ovchinnikov, Nat. Commun. **9**, 919 (2018).
[11] D. Yan, S. Wang, Y. Lin, G. Wang, Y. Zeng, M. Boubeche, Y. He, J. Ma, Y. Wang, D.-X. Yao, and H. Luo, J. Phys.: Condens. Matter **32**, 025702 (2020).
[12] Y. Liu, Y. Gao, S. Zhang, J. He, J. Yu, and Z. Liu, Nano Res. **12**, 2695 (2019).

[13] N. Zibouche, A. Kuc, J. Musfeldt, and T. Heine, Ann. Phys. **526**, 395 (2014).

[14] K. L. Mak, K. F. McGill, J. Park, and P. L. McEuen, Science **344**, 1489 (2014).

[15] D. Xiao, W. Yao, and Q. Niu, Phys. Rev. Lett. **99**, 236809 (2007).

[16] S. Bhowal and S. Satpathy, Phys. Rev. B **101**, 121112(R) (2020).

[17] L. M. Canonico, T. P. Cysne, A. Molina-Sanchez, R. B. Muniz, and T. G. Rappoport, Phys. Rev. B **101**, 161409(R) (2020).

[18] T. P. Cysne, M. Costa, L. M. Canonico, M. B. Nardelli, R. B. Muniz, and T. G. Rappoport, Phys. Rev. Lett. **126**, 056601 (2021).

[19] S. Bhowal and G. Vignale, Phys. Rev. B **103**, 195309 (2021).

[20] D. Xiao, G.-B. Liu, W. Feng, X. Xu, and W. Yao, Phys. Rev. Lett. **108**, 196802 (2012).

[21] Q. Ma, S.-Y. X. H. Shen, D. MacNeill, V. Fatemi, T.-R. Chang, A. M. M. Valdivia, S. Wu, Z. Du, C.-H. Hsu, S. Fang, Q. D. Gibson, K. Watanabe, T. Taniguchi, R. J. Cava, E. Kaxiras, H.-Z. Lu, H. Lin, L. Fu, N. Gedik, and P. Jarillo-Herrero, Nature (London) **565**, 337 (2019).

[22] I. Sodemann and L. Fu, Phys. Rev. Lett. **115**, 216806 (2015).

[23] Z. Z. Du, C. M. Wang, H.-Z. Lu, and X. C. Xie, Phys. Rev. Lett. **121**, 266601 (2018).

[24] M.-S. Qin, P.-F. Zhu, X.-G. Ye, W.-Z. Xu, Z.-H. Song, J. Liang, K. Liu, and Z. Liao, Chin. Phys. Lett. **38**, 017301 (2021).

[25] V. Vargiamidis, P. Vasilopoulos, M. Tahir, and N. Neophytou, Phys. Rev. B **102**, 235426 (2020).

[26] B. T. Zhou, K. Taguchi, Y. Kawaguchi, T. Yukio, and K. Law, Commun. Phys. **2**, 26 (2019).

[27] C. Zhao, P. Norden, T. and Zhang, P. Zhao, Y. Cheng, F. Sun, J. P. Parry, P. Taheri, J. Wang, Y. Yang, T. Scrace, K. Kang, S. Yang, G. X. Miao, R. Sabirianov, G. Kioseoglou, W. Huang, A. Petrou, and H. Zeng, Nat. Nanotechnol. **12**, 757 (2017).

[28] H. Da, Q. Song, P. Dong, H. Ye, and X. Yan, J. Appl. Phys. **127**, 023903 (2020).

[29] T. Habe and M. Koshino, Phys. Rev. B **96**, 085411 (2017).

[30] J. Hidding and M. H. D. Guimarães, Frontiers Mater. **7**, 594771 (2020).

[31] P. Gambardella and I. M. Miron, Philos. Trans. R. Soc. A Math. Phys. Eng. Sci. **369**, 3175 (2011).

[32] D. MacNeill, G. M. Stiehl, M. H. D. Guimaraes, R. A. Buhrman, J. Park, and D. C. Ralph, Nat. Phys. **13**, 300 (2017).

[33] F. Xue, C. Rohmann, J. Li, V. Amin, and P. Haney, Phys. Rev. B **102**, 014401 (2020).

[34] T. Miyamachi, T. Schuh, T. Märkl, C. Bresch, T. Balashov, A. Stöhr, C. Karlewski, S. André, M. Marthaler, M. Hoffmann, M. Geilhufe, S. Ostanin, W. Hergert, I. Mertig, G. Schön, A. Ernst, and W. Wulfhekel, Nature (London) **503**, 242 (2013).

[35] F. Donati, S. Rusponi, S. Stepanow, C. Wäckerlin, A. Singha, L. Persichetti, R. Baltic, K. Diller, F. Patthey, E. Fernandes, J. Dreiser, Ž. Šljivančanin, K. Kummer, C. Nistor, P. Gambardella, and H. Brune, Science **352**, 318 (2016).

[36] R. Baltic, M. Pivetta, F. Donati, C. Wäckerlin, A. Singha, J. Dreiser, S. Rusponi, and H. Brune, Nano Lett. **16**, 7610 (2016).

[37] A. Shick and A. Lichtenstein, J. Magn. Magn. Mater. **454**, 61 (2018).

[38] A. Shick and A. Denisov, J. Magn. Magn. Mater. **475**, 211 (2019).

[39] [https://www.flapw.de/]

[40] A. B. Shick, A. I. Liechtenstein, and W. E. Pickett, Phys. Rev. B **60**, 10763 (1999).

[41] J. P. Perdew, K. Burke, and M. Ernzerhof, Phys. Rev. Lett. **77**, 3865 (1996).

[42] P. Kurz, G. Bihlmayer, and S. Blügel, J. Phys.: Condens. Matter **14**, 6353 (2002).

[43] I. L. M. Locht, Y. O. Kvashnin, D. C. M. Rodrigues, M. Pereiro, A. Bergman, L. Bergqvist, A. I. Lichtenstein, M. I. Katsnelson, A. Delin, A. B. Klautau, B. Johansson, I. Di Marco, and O. Eriksson, Phys. Rev. B **94**, 085137 (2016).

[44] F. Freimuth, Y. Mokrousov, D. Wortmann, S. Heinze, and S. Blügel, Phys. Rev. B **78**, 035120 (2008).

[45] A. A. Mostofi, J. R. Yates, G. Pizzi, Y.-S. Lee, I. Souza, D. Vanderbilt, and N. Marzari, Comput. Phys. Commun. **185**, 2309 (2014).

[46] See Supplemental Material at http://link.aps.org/supplemental/10.1103/PhysRevB.106.064401 for further analysis on orbital contributions.

[47] N. D. Mermin and H. Wagner, Phys. Rev. Lett. **17**, 1133 (1966).

[48] R. B. Griffiths, Phys. Rev. **136**, A437 (1964).

[49] J. M. Luttinger, Phys. Rev. **81**, 1015 (1951).

[50] D. Wortmann, S. Heinze, P. Kurz, G. Bihlmayer, and S. Blügel, Phys. Rev. Lett. **86**, 4132 (2001).

[51] G. T. Rado and H. Suhl (eds.), *Magnetism* (Academic Press, New York, 1963), p. ii.

[52] L. M. Sandratskii, Phys. Stat. Solidi B **136**, 167 (1986).

[53] P. Kurz, F. Förster, L. Nordström, G. Bihlmayer, and S. Blügel, Phys. Rev. B **69**, 024415 (2004).

[54] Y. A. Bychkov and É. I. Rashba, JETP Lett. **39**, 78 (1984).

[55] A. Manchon, H. C. Koo, J. Nitta, S. M. Frolov, and R. A. Duine, Nat. Mater. **14**, 871 (2015).

[56] S. R. Park, C. H. Kim, J. Yu, J. H. Han, and C. Kim, Phys. Rev. Lett. **107**, 156803 (2011).

[57] J. H. Park, C. H. Kim, H. W. Lee, and J. H. Han, Phys. Rev. B **87**, 041301(R) (2013).

[58] D. Go, J.-P. Hanke, P. M. Buhl, F. Freimuth, G. Bihlmayer, H.-W. Lee, Y. Mokrousov, and S. Blügel, Sci. Rep. **7**, 46742 (2017).

[59] V. Sunko, H. Rosner, P. Kushwaha, S. Khim, F. Mazzola, L. Bawden, O. J. Clark, J. M. Riley, D. Kasinathan, M. W. Haverkort, T. K. Kim, M. Hoesch, J. Fujii, I. Vobornik, A. P. Mackenzie, and P. D. C. King, Nature (London) **549**, 492 (2017).

[60] D. Go, D. Jo, C. Kim, and H. W. Lee, Phys. Rev. Lett. **121**, 086602 (2018).

[61] D. Go, D. Jo, T. Gao, K. Ando, S. Blügel, H. W. Lee, and Y. Mokrousov, Phys. Rev. B **103**, L121113 (2021).

[62] X. Xu, W. Yao, D. Xiao, and T. F. Heinz, Nat. Phys. **10**, 343 (2014).

[63] J. P. Perdew and A. Zunger, Phys. Rev. B **23**, 5048 (1981).

[64] A. Shick, A. Lichtenstein, D. S. Shapiro, and J. Kolorenc, Sci. Rep. **7**, 2751 (2017).

[65] C. Godfrin, R. Ballou, E. Bonet, M. Ruben, S. Klyatskaya, W. Wernsdorfer, and F. Balestro, npj Quantum Inf. **4**, 53 (2018).

[66] S. Bertaina, S. Gambarelli, A. Tkachuk, I. Kurkin, B. Malkin, A. Stepanov, and B. Barbara, Nat. Nanotechnol. **2**, 39 (2007).

[67] M. Grimm, A. Beckert, G. Aeppli, and M. Müller, PRX Quantum **2**, 010312 (2021).

[68] A. Kinos, L. Rippe, S. Kröll, and A. Walther, Phys. Rev. A **104**, 052624 (2021).